Mapping a novel metric for Flash Flood Recovery using Interpretable Machine Learning

Anil Kumar,[a] Manabendra Saharia,[a,b] Pierre Kirstetter,[c]

[a] *Department of Civil Engineering, Indian Institute of Technology Delhi, Hauz Khas, New Delhi 110016, India*

[b] *Yardi School of Artificial Intelligence, Indian Institute of Technology Delhi, Hauz Khas, New Delhi 110016, India*

[c] *School of Meteorology, University of Oklahoma, Norman, Oklahoma, 73019, United States*

Corresponding author: Dr. Manabendra Saharia, msaharia@iitd.ac.in

ABSTRACT

Flash floods are one of the most devastating natural disasters, yet many aspects of their severity and impact are poorly understood. The recession limb is related to post-flood recovery and its impact on communities, yet it remains less documented than the rising limb of the hydrograph to predict the peak discharge and timing of floods. . This work introduces a new metric called the flash flood recovery or recoveriness, which is the potential for recovery of a watershed to pre-flood conditions. Using a comprehensive database of 78 years and supervised machine learning algorithms, flash flood recovery is mapped in the conterminous United States. A suite of geomorphological and climatological variables is used as predictors to provide probabilistic estimates of recoveriness. Slope index, river basin area and river length are found to be the most significant predictors to predict recoveriness. Several new localized hotspots were identified, such as the western slopes of the Appalachians consisting of Kentucky, Tennessee, and West Virginia and the interlinked areas of western Montana and northern Idaho. This new metric can be useful for prioritizing relief and rehabilitation efforts as well as precautionary measures for disaster risk reduction.

1. Introduction

Accounting for one-third of all global geophysical disasters, floods cause substantial damage to agriculture, infrastructure, human life, and the socioeconomic system (Berz 2000; Douben 2006; Rentschler et al. 2022). Although total flood damage caused nationally in the United States varies from year to year, there has been a statistically notable increasing trend of 2.92% per year in the 20th century (Pielke and Downton 2000). In the water year 2021-22 alone, 102 flood related deaths and direct flood damages of $2.8 billion have been reported in the United States (2022). A comprehensive large-sample characterization of floods in the United States revealed that the fastest responding flash floods were caused by intense monsoon thunderstorms and steep terrain in the arid Southwestern US (Saharia et al. 2017a). Globally, streamflow extremes are characterized by various hydrogeomorphic factors such as annual precipitation, precipitation of wettest month and quarter, basin magnitude, first-order streams length, basin perimeter, and drainage area (Kuntla et al. 2022). A new variable called flashiness was proposed for quantifying flash flood severity of such severe events using a multitude of geophysical and climatological variables (Saharia et al. 2017b). Most prognostic

efforts in hydrology are dedicated towards understanding and predicting peak discharge and rise time of flooding, while very little research is available on the recession limb of the hydrograph, including non-availability of metrics describing the recovery of a watershed to pre-flood conditions.

Understanding and predicting flood hydrograph is the overarching goal of the field of hydrology. A flood hydrograph consists of a rising and a falling limb. At the event scale, the rising limb rate of a watershed was found to be correlated with the maximum rainfall intensity and the elapsed time of rainfall centroid (Shuster et al. 2008). Potdar et al. (2021) found that the spatial organization of rainfall influences the basin response on par with the geomorphology and climatology of flash flood generating basins. The rising limb of the flood hydrograph is related to extreme events such as flash floods, while the recession part of the curve is concerned with water drainage (Shorr 2000). The recession curve is typically longer than 50 percent of an entire flooding event due to a copious supply of water resources during the entire flood event (Ahmad et al. 2014; Liu et al. 2015). In operational flood forecasting, the crossing of different river stages (action/minor/moderate) activates different types of procedural responses from local responders, and restoration of a watershed to pre-flood conditions is dependent on how fast the river flow can return below the breached river stage. Despite this, much of hydrology research is focused on the rising limb, specially predicting the peak discharge and timing of a flood, while the recession period of floods, although being crucial for relief and recovery of communities, post-flooding health and environmental concern, has gained less attention. A multitude of metrics have been developed to assess the severity of floods (Saharia et al. 2017b; Baker et al. 2004; Diakakis et al. 2020; Alfieri and Thielen 2015) but based on our current knowledge, no such metric exists for recovery of a watershed to pre-flood conditions, i.e. flood recovery.

A few researchers have explored the relationship between the recession period and physical predictors. According to Khaleghi et al., (2011), in mountainous regions, the two main predictors responsible for the flood recovery period are 1) rainfall and 2) underlying surface conditions. Ground surface conditions also affect the flood recession process (Chang and Feng 2017; Costa et al. 2003). Conversely, transformation of grassland or cultivated land into urban areas would lead to rise in flood peak flow, thereby increasing the recovery period. Another factor affecting the flood recovery period is terrain slope. For example, in the slope experiment presented by Shixiang & Shaowen, (1991), the impact on the recession flow

drops rapidly with a slope exceeding 9 degrees, and greater impact is expected when the slope value is below 9 degrees, suggesting that 9 degrees is a critical value. Studies such as Ye et al. (2019) discuss how the river cross-section affects the recession period and flow. Amit et al. (2002) found that the main factor affecting the recession curve in perennial springs are the aquifer lithology and the geometry of the water conduits. Biswal & Marani (2010) suggested a link between recession curves and the topology of a river network. Bhaskar et al. (2000), defined an index based on flood hydrograph shape characteristics such as magnitude ratio, gradient of the rising curve and the response time of the flash flood to differentiate between floods and flash floods. Evaluation of various techniques for base-flow and recession analyses was done by Nathan & McMahon (1990) and Chapman (1999), where they showed that the linear storage model can be used as a very good approximation in most cases by comparing algorithms for streamflow recession.

Though the literature on baseflow recession curves is extensive, none of the metrics and techniques developed are based on the actual definition of floods used by operational agencies such as the US National Weather Service (NWS). NWS has pre-defined flood stages at thousands of gauging stations across the country, established in cooperation with local public officials. Once the river reaches the flood stage, NWS declares a minor, moderate, or a major flood, with each category defined based on property damage and public threat. Thus, a metric for flood recovery tied to operational definitions of floods and flash floods has the potential for wide usage. Apart from developing this metric at designated gauge stations, this metric is required at every watershed so that flood recovery can be monitored in ungauged locations.

In this paper, we have introduced a new index for flash flood recovery, called the "Recoveriness", based on a large observational dataset. Further, we have mapped recoveriness to every watershed in the United States on a continuous grid using a machine learning based approach on a multitude of predictors related to basin climatology and geomorphology. Further, an interpretable machine learning framework called SHAP (SHapley Additive exPlanations) has been used to quantify the relative impact of the causative hydrogeomorphic factors behind recoveriness. The study is organized as follows: Section 2 describes the data sources and methods that have been applied, Section 3 describes the machine learning methods and interpretation methodology, Section 4 characterizes

recoveriness based on a multitude of variables and maps it over continental United States. Finally, Section 5 provides a summary of the findings and concluding remarks.

2. Study area and data source

a. Datasets

This study uses the Unified flash flood database (Gourley et al. 2013). which is a compilation of carefully selected data from various sources such as the USGS streamflow data, NWS flashflood reports, and a storm event database. The Unified Flash Flood Database is further enhanced by public survey response data collected during the Severe Hazards Analysis and Verification Experiment (SHAVE) described by Ortega et al. (2009) and the event-scale rainfall spatial variability (Saharia et al. 2021).

The USGS conducts automated collection of instantaneous streamflow information at every 5 – 60 min interval for 10,106 gauges distributed over the U.S. A coordinated approach by NWS with the USGS and local stakeholders has resulted into defining various categories of flooding such as minor, moderate, and major in addition to establishing crucial flood level stages like the action stage. This comprehensive approach is applied to the streamflow gauges at 3490 locations. Well-defined threshold levels have been defined for a specific set of gauges within the USGS network, which forms a significant input for various applications including modeling. The term “Action stage” denotes the level at which the NWS could initiate measures for a possible adverse hydrologic event. The stage mostly appears with conditions indicative of the bank full cases (2019).

Interestingly, around 41% of the USGS stations display the same values for the action and bank full stages with a mean variation of 1.3%. Data reliability is further ensured with USGS providing regulations for the stations vulnerable to human alterations and diversions leaving us with 70,596 flooding events from 1649 unique monitoring stations. By convention, the USGS characterizes flood events when the streamflow exceeds a predefined action stage for each gauge in its network. Further, events must be separated by at least 24h to be counted as independent events in the unified flash database. Essential details are already specified in the core database. For each gauge in the network, the following are specified: unique identifier (ID) for each gauge, the latitude and longitude based geographical coordinates, initiation time (UTC) that marks the exceedance of the flow above the action stage threshold, conclusion

time (UTC) that marks the recession below the threshold, the peak flow magnitude (m^3s^{-1}), the time at which the peak was attained (UTC), and the flood rise time, i.e., the interval between the discharge when it surpassed the threshold and the when it attained the peak (hours).

b. Recoveriness as a metric of flood recovery

According to the NWS, flash floods are said to have occurred when there is an intense rise in water level in an area that typically remains arid or when the water level surpasses the predefined flood threshold in the case of a stream or a creek. This can happen within 6 hours from the beginning of situations like dam break, heavy rainfall, and water flow obstruction due to ice.

This work introduces a novel metric called the recoveriness for measuring flood recovery. We define "Recoveriness" in Equation (1) to be the ratio of the difference between the peak discharge and the action stage discharge, divided by the time it takes for the flooding to return to the action stage, and the basin area. As it can be seen in Figure 1, the metric characterizes the rate of decline of the hydrograph from its peak position, consequently capturing both the magnitude and timing components. Higher values signify accelerated recovery to pre-flood conditions. If ψ denotes recoveriness, the gauging station numbers as S, and the number of events as N_i (for gauge i), where i ranges from 1 to S, then, the recoveriness for a j^{th} event can be expressed as in Equation (1):

$$\psi_{ij} = \frac{Q_{ij}^{(p)} - Q_{ij}^{(a)}}{A_i T_{ij}} \tag{1}$$

$Q^{(p)}$ in the above equation represents the peak discharge, $Q^{(a)}$ represents the action stage discharge, the basin area is represented with A, and T represents the recession time. To normalize these values between 0 and 1, an empirical cumulative distribution function (ECDF) is utilized as depicted in Equation (2). The standardized version of recoveriness ($\emptyset$) is given by:

$$\tilde{\phi}_{ij} = \frac{1}{\sum_{i=1}^{S} N_i} \sum_{i=1}^{S} \sum_{j=1}^{N_i} I_{(\phi_{ij} \leq t)} \tag{2}$$

where t is the ranked value of recoveriness, $I_{(E)}$ is the indicator function yielding 1 if the condition E is true and 0 otherwise. Event level recoveriness is calculated by Equation (2).

The standardized recoveriness for a given basin i, the median value of computed recoveriness can be given using Equation (2) for all events N_i observed at that gauge station.

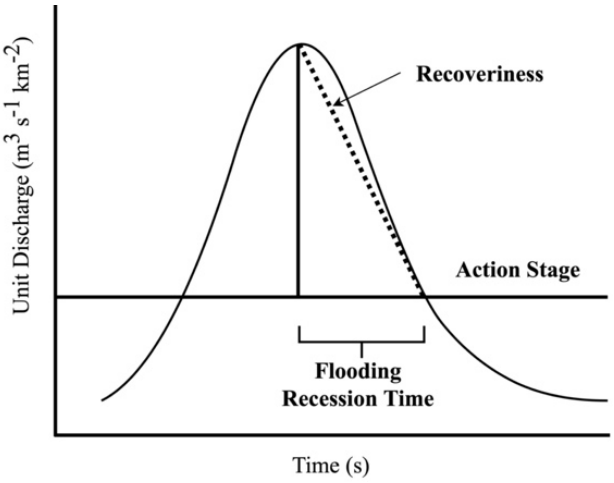

Fig. 1. Graphical representation of recoveriness - part right of the peak of the graph.

High recoveriness values are a fingerprint of rapid (transient) hydrological processes that are efficient at transferring water across the watershed. It translates also into high capability to concentrate water at the watershed outlet which is associated with high flashiness (Saharia et al. 2017b). The definition of recoveriness involves the discharge terms $Q^{(p)}$, $Q^{(a)}$ in the numerator and the area, recession time in the denominator. Table 1 illustrates how recoveriness varies as a function discharge, area, and time and how it can be interpreted. The highest recoveriness is achieved when $\boldsymbol{Q_{diff.}}$ is high while area, time are low. Conversely, if $\boldsymbol{Q_{diff.}}$ is low while area and recession times are high, we expect the slowest watershed recovery. A recoveriness value of 0 – 0.25 reflects slow recovery, 0.25 – 0.75 for moderate recovery, and 0.75 – 1 for rapid recovery.

$\boldsymbol{Q_{diff.}}$ $\boldsymbol{(m^3 s^{-1})}$	**Area** $\boldsymbol{(km^2)}$	**Time** (months)	**Recoveriness**	**Interpretation**
0.65 Low	150.0 Low	1.0 Low	0.66	Moderate
0.65	150.0	6.0	0.33	Moderate

Low	Low	High		
0.65 Low	500.0 High	6.0 High	0.16	Slow
11.50 High	150.0 Low	1.0 Low	1.00	Rapid
11.50 High	150.0 Low	6.0 High	0.83	Rapid
11.50 High	500.0 High	6.0 High	0.50	Moderate

Table 1. Recoveriness indicator.

In simple terms, recoveriness can be thought of as the system's capacity to rebound from a flood event to pre-flood conditions. The index bears a nonlinear relationship with its 14 predictors shown in Table 2. For instance, the $Q^{(p)}$ term readily encapsulates the effect of precipitation and rainfall as they can directly escalate its value which consequently manifests in the computation of recovery. Similarly, temperature can affect the melting times of snow again effecting $Q^{(p)}$. Water retention and runoff are determined by slope index and rock volume; the drainage efficiency is determined by the outlet slope and the relief ratio; elevation and area are concerned with water input and flow; soil infiltration and transport are affected by the river length; curve number, rock depth, and texture determine the runoff rates. The collective effect of all these variables are embedded in the hydrograph and the recoveriness index facilitates with a quantity that is easy to interpret.

As per the definition provided, observed recoveriness is derived across the US as shown in Figure 2. Several regional hotspots can by visually identified with high recoveriness: 1) the West Coast, 2) Arizona, 3) the Front Range, 4) Flash Flood Alley, 5) the Missouri Valley, and 6) the Appalachians. As recoveriness directly depends on geomorphology and topology of the watershed, high recoveriness in these six regions can be explained by examining those predictors. In the west coast, the high recoveriness values could be due to the ridge tops and steep slopes on the western side of the Sierra Nevada Mountain range which obstructs the Northern Pacific moisture-laden air moving eastward. Secondly, high recoveriness values are observed in the basins in Arizona ranging from the Northern higher terrain plateau to the

lower deserts in the South-Eastern Arizona. This is due to the high slopes of the front range of the Rocky Mountain range capturing the moisture traveling from the Gulf of Mexico, e.g., during the American Monsoon. High recoveriness is also observed in the urban corridor covering Austin, San Antonio, and Waco along the Balcones Escarpment in Texas (Flash flood alley). A secondary cluster can be observed near the Gulf Coast close to Houston. The recoveriness increases as one moves farther towards the northeast following the Ozarks regions and maximizes in and around the center of Missouri. Also, in the eastern United States, from Georgia to Maine in and around the Appalachians, high recoveriness values are also observed.

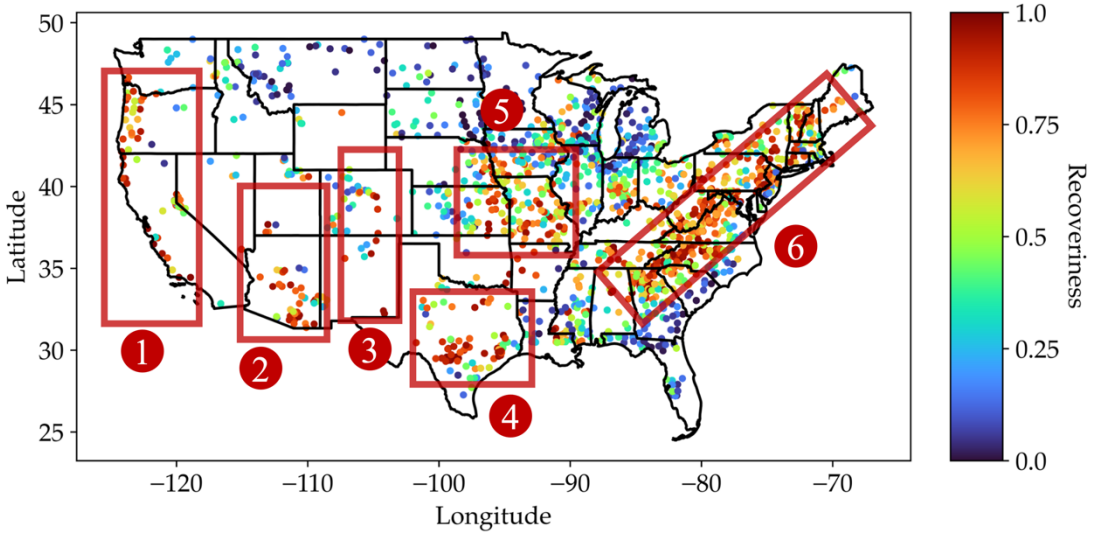

Fig. 2. Map of the United States showing the spatial distribution of recoveriness. The bounded boxes denote the following regions: 1) the West Coast, 2) Arizona, 3) Front Range, 4) Flash Flood Alley, 5) Missouri Valley, 6) the Appalachians.

3. Methodology

In this study, the Random Forest Quantile Regressor (RFQR) has been used as the supervised learning algorithm for regression between recoveriness and the multitude of hydrogeomorphic predictors. The complete methodology of the study covering data preparation, train-test split, hyperparameter tuning, performance evaluation, and model interpretation has been explained in Figure 3. The dataset is divided into a training and a testing set (4:1 ratio) for a supervised learning analysis.

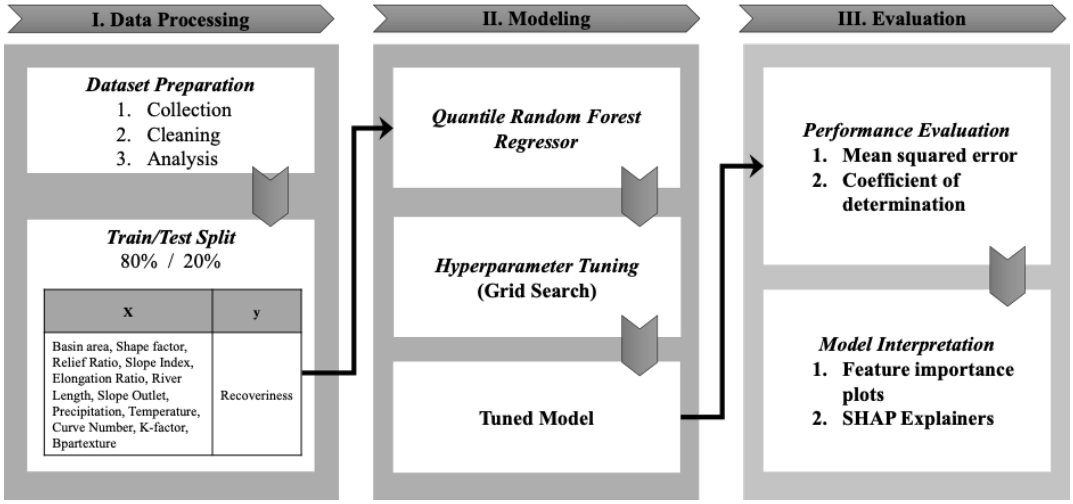

Fig. 3. Methodology for the computation of observed and predicted recoveriness. See Table 2 for a description of variables.

Grid search is a widely used technique for hyperparameter tuning where the training algorithm is tested for its performance at different combinations (grid) of hyperparameter values. The scheme naturally avoids any exhaustive search step while providing the best combination from the set. Therefore, for tuning the algorithm, a grid search is performed, of which we only report the final and optimal set of hyperparameters of the model here. The mean squared error and coefficient of determination metrics are used to evaluate model performance. Model interpretation is performed using SHAP (SHapley Additive exPlanations), which is a game theoretic approach to explain the output of any machine learning model (Lundberg and Lee 2017).

a. Hydrogeomorphic Predictors

A total of 14 physical variables have been derived from various datasets at the watershed scale in and used as predictors this study. The list of predictors and their description in the context of floods is provided in Table 2.

- The area (**area**) of the watershed is important as larger areas usually collect more water/runoff.
- The elongation length (**el**) and shape factor (**k**) affect the time and speed with which water is channeled into nearby water bodies like rivers.
- River length (**rl**) can play a dual role – while elongated regions may appear more prone to flooding, they may also allow more time for assessment.

- Relief ratio (**rr**), slope at the outlet (**slopeoutlet**), and slope index (**si**) are indicative of steepness of the watershed and terrain.
- Climatologic variables such as precipitation (**precip**) and temperature (**temp**) also impact floods. The risk is high with higher rainfall, and with higher temperatures, the snowmelt is faster.
- Infiltration into the ground and runoff are determined by soil and rock predictors such as the k-factor (**k-fact**), rock depth (**rd**), and rock volume (**rv**).

The soil texture (**bpartexture**) and the curve number (**cnbasin**) are indicative of infiltration rates and direct runoff, respectively.

Sr. No.	Hydrogeomorphic Predictor	Description
1.	Area (area)	Watershed area contributing to runoff.
2.	Elongation length (el)	How long the watershed is.
3.	Shape factor (k)	A dimension-less quantity which is equal to watershed area divided by the square of the channel length
4.	River length (rl)	The river length can be defined as the distance measured along the line that connects the watershed outlet to the point where the watershed's boundary meets the river's main channel.
5.	Relief ratio (rr)	The relief ratio is defined as the elevation difference between a watershed's lowest point and its highest point to the watershed's length, directly affecting both the runoff and the speed of flood rising speed.
6.	Slope index (si)	A quantity calculated from the slopes at 10% and 85% of length of the main channel in the upstream direction starting from the mouth of the watershed (Saharia et al., 2017b)
7.	Slope outlet (slopeoutlet)	Computed slope at a distance of 1 km from the watershed outlet
8.	Precipitation (precip)	Precipitation
9.	Temperature (temp)	Temperature

Table 2. Description of the variables.

As a first-hand examination of data, the Pearson correlation coefficient matrix is computed for the entire data. The formula for the Pearson correlation coefficient is given by:

$$r_{xy} = \frac{\sum_{i=1}^{n}(x_i - \bar{x})(y_i - \bar{y})}{\sqrt{\sum_{i=1}^{n}(x_i - \bar{x})^2 \sum_{i=1}^{n}(y_i - \bar{y})^2}} \quad (3)$$

In Equation (3), r_{xy} denotes the correlation coefficient between the x and y. The means of the two variables are denoted by $\bar{x}, \bar{y}$. Application of the above formula on the input data produces Figure 4 – a heatmap indicative of the correlation coefficient among all pairs of variables. Apart from a high correlation with themselves, the following variable pairs show a correlation higher than 0.5 – (area, river length), (relief ratio, slope outlet), (relief ratio, slope index), (elongation, shape factor). Regarding the output variable, recoveriness (mr.ecdf), following variables are least correlated – curve number, temperature, and Bpar Texture. The blue and green regions in the heatmap represent zero to negatively correlated pairs. The dendrogram represents the closeness among different variables. The dendrogram above the heatmap shows the clusters formed among combinations of variables. Predictor pairs that branch-in together show closer association with similar information.

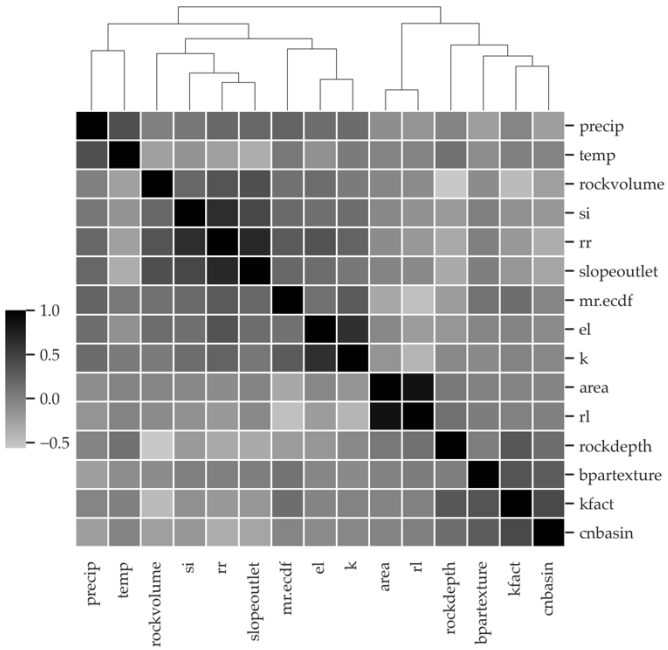

Fig. 4. Pearson correlation coefficient showing the correlation among different input variables.

b. Shapely values

Originating from the cooperative game theory, the "shapely" values are a way to assign value to individual contributor from the total value created from the coalition. The **SH**apely **A**dditive Ex**p**lanations (SHAP) is a global feature interpretation method based on shapely values which can be used to interpret the relative impact of predictors on model outputs machine learning. The following formula is used to compute the SHAP values:

$$\phi_i(x) = \sum_{S \subseteq N \setminus \{i\}} \frac{|S|!\,(|N| - |S| - 1)!}{|N|!} \left(f_x(S \cup \{i\}) - f_x(S)\right) \quad (4)$$

In the above formula, ϕ_i is the SHAP value for i^{th} predictor and x instance; N is the complete predictor set and S is set of predictors excluding the i^{th} predictor; $f_x(S \cup \{i\})$ is the prediction of the model including the i^{th} predictor in subset S for the x input. $f_x(S)$ is the prediction of the model when only including predictors in subset of S for x input.

c. Random Forest Quantile Regression (RFQR)

The relationship between a hydrograph variable (recoveriness) and hydrogeomorphic controls is complex and non-linear. Tree-based methods have been particularly successful in modeling such relationships in hydrology since their versatility can be attributed to their capability of handling nonlinearity (Ao et al. 2019; Babagoli et al. 2019; Huan et al. 2020), explainability (Gimeno et al. 2023; Islam et al. 2020; Joshi et al. 2023; Nanfack et al. 2022) and robustness towards outliers in data (Buschjäger et al. 2022; John 1995; Marcuzzi et al. 2022; Panjei et al. 2022). Since, our objective is to model recoveriness ib observed locations, map it to ungauged locations, and provide an estimate of uncertainty, we selected the Random Forest Quantile Regression (RFQR) algorithm (Meinshausen and Ridgeway 2006). RFQR are an extension of the Random Forest (RF) algorithm that can model the statistical distribution of the target variable, allowing us to provide quantile estimates of the predicted values. Interval estimates in RFQR provide quantiles that help gain a more complete picture of the potential outcomes in the target. Markov chain Monte Carlo-based methods also exist when it comes to making probabilistic estimates about the dependent variable (Amaya et al. 2022; Kumar et al. 2020; Yan et al. 2020). However, scaling them to large datasets poses an issue; therefore, we opt for the Random Forest Quantile Regression algorithm.

During the training stage, while the conventional RFs only store summary statistics such as the mean and mode of the training samples, RFQR stores all the samples reaching the

terminal nodes. At the prediction stage, RFQR uses these stored samples to construct an empirical cumulative distribution function (ECDFs) which is later used to predict the quantiles for new data points. Thus, any quantile can be queried based on these CDFs.

The algorithmic steps of RFQR can be described as follows:

- Bootstrap sampling: Create bootstrap samples from the original data
- Build Decision Tree: For each of such bootstrap partition, build a Decision tree using the mean squared criterion (for regression problems)
- Leaf node prediction: Store all the data points reaching the leaf node to enable quantile computation
- Voting: During prediction get the votes from each tree to predict the quantile estimate for the new data point

As the recoveriness variable bears a nonlinear relationship with the predictors (Table 2, Figure 4), it is important to model the entire statistical distribution of the target variable and not just summary statistics.

4. Results and Discussions

a. Hydrogeomorphic controls on Recoveriness

Recoveriness is a highly complex and non-linear function of geomorphological and climatological predictors of a watershed. The various hydrogeomorphic controls include annual precipitation, watershed area, ruggedness, k-factor, rock depth, curve number of the watershed etc. The spatial distributions of important climatological and geomorphological variables is summarized in Figure 5. By comparison with the recoveriness spatial distribution in Figure 2, with some notable exceptions in the extreme west coast of Washington and Oregon county (marked red), the area is characterized by high recoveriness in the Pacific northwest and towards the southeast near the Appalachians Figure 5a). Arizona, although being more arid than other flashy regions, exhibits several high recoveriness areas.

The runoff response to excess rainfall can be characterized by the basin curve number. Many predictors affect this variable, including land cover and hydrologic soil group that help approximate runoff generation basing infiltration, vegetative interception, and soil moisture

retention. It varies in the range 30 to 100, with higher values indicating higher runoff potential. In Figure 5b), we observe a high runoff potential in the Flash Flood Alley and Missouri. It is expected to be highly correlated with the recoveriness due to the presence of a combination of steep terrains and impermeable soils. In Figure 5c) the slope index is representative of the DEM-derived slope computed along the basin length (Costa 1987).

Regions like the Appalachians, Sierra Nevada, and Arizona show high recoveriness due to the presence of higher slopes with a few exceptions where high values are observable in flat regions as well. In Figure 5d), some notable clusters of gauged catchments can be observed on the border of Nevada and California near the Tahoe Lake, as well as some midwestern areas like Indianapolis and St. Louis and extending along the Appalachian regions towards densely populated northeastern United States. Due to the presence of small catchments, the watersheds are bound to possess high recoveriness values – as evident upon comparison with Figure 2.

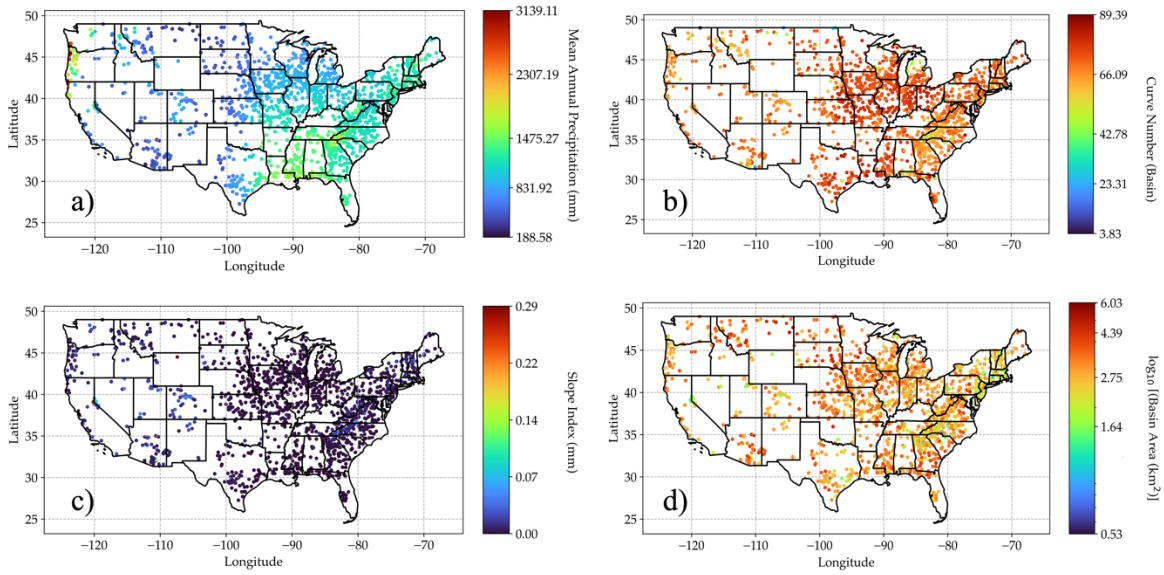

Fig. 5. Scatter plot showing the distribution of (a) mean annual precipitation, (b) curve number , (c) slope index, and (d) logarithm of watershed area across continental US.

The influence of geomorphological and climatological predictors such as basin area, average annual rainfall, steepness of the terrain or slope index, and curve number on recoveriness have been examined using quantile plots (Figure 6). In the current context, a quantile plot gives information about the correlation and variability in the relationship

between the predictor variable and recoveriness. Each plot shows 1st through 99th quantiles for specific ranges of the predictor. The first-order dependency is revealed by the conditional median or the 50th quantile; the remaining ones can serve as estimates of the uncertainty in the relationship. Extreme values of recoveriness can be determined by excluding the interquartile range between the 10th and 90th quantiles.

Figure 6a) shows the variation of recoveriness with respect to the watershed area. One can observe that there is a gradual decrease in recoveriness with increasing area, as expected since larger basins are expected to display slower dynamics than smaller basins. Figure 6b) shows the variation of recoveriness with mean annual precipitation. Clearly, there is a conditional relationship between recoveriness and mean annual precipitation which appears to be constant below 1000 mm, after which it increases slightly and then decreases. This is suggestive of a threshold effect. Figure 6c) shows the variation of recoveriness against slope index, which display a clear increasing relationship till a threshold value. Recoveriness is increasing with slope index for slope index values below 0.3 (higher slope is associated with faster transfer of water) and for higher values, recoveriness bears an almost constant relation with this geomorphologic variable. The relation of the basin curve number (CN) and recoveriness is shown in Figure 6d). Recoveriness shows a varying degree of correlation with the 4 predictors which are deemed important in most hydrological data modeling. A positive correlation in case of slope index, is indicative that basins with steeper topography generally experience quick recovery, hence high recoveriness with greater maximum flow rates and quicker decline times. Similarly, basin area shows the inverse trend of the similar magnitude. The plot also explains the fact that basins with smaller catchment area are expected to recover faster. Though the quantile curves provide valuable information about the relationship recoveriness exhibits with individual predictors, flood processes in reality result from complex interactions between a large number of variables. Thus, we adopt a multidimensional modeling approach using random forest quantile regressor to uncover the collective and individual impact of these large number of predictors on recoveriness.

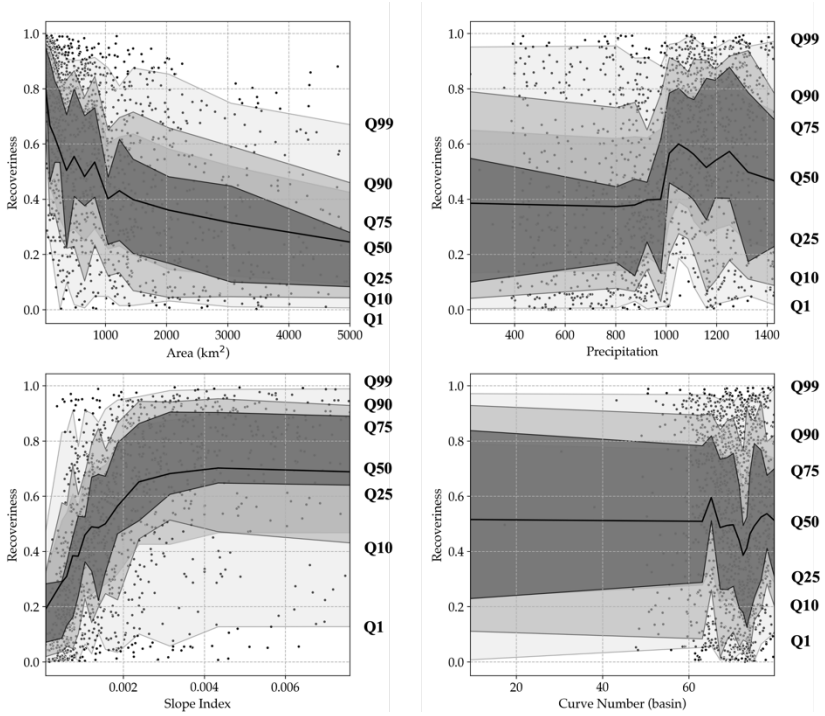

Fig. 6. Plots showing recovery percentiles from the first to the ninety-ninth, for following variables: (a) mean annual precipitation, (b) curve number, (c) slope index, and (d) basin area

b. Multidimensional modeling of recoveriness

The RFQR model consists of a total of 10 Decision Trees – Figure 7 shows two participating Decision Trees that can vote for the outcome during prediction. We can see that the slope index (si) variable happens to occupy the root node making it the most important variable. The Random Forest algorithm evaluates this predictor's values to be most informative in forming the bifurcation at the root level. The threshold value of "si" is computed to be 0.0. The "true" branch leads to the "area" node and the "false" branch to the precipitation node. Upon analysis, it was found that 9 out of 10 decision trees preferred the structure shown in Figure 7a), helping it to discover the relationship (nonlinear) among the different predictors.

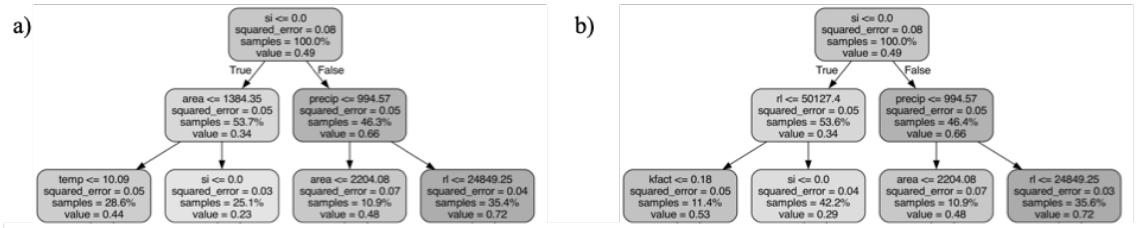

Fig. 7. Nonlinear dependence of "Recoveriness" on predictors: The Random Forest consisted of 10 Decision Trees. The bifurcation in the predictor space tends to follow the above two structures: a) This structure occurs 9/10 times, and b) This structure occurs 1/10 times, showing that Slope Index (si) is the most important variable followed by Area, Precipitation and River length. The depth of the trees has been truncated to level 3 although deeper layers were involved in the model.

The deeper branches still model more complex relationships among the predictors. We only show the first three levels of the trees here.

	MSE	R^2
Training	0.010	0.866
Testing	0.011	0.865

Table 3. Training and testing results.

Figure 7b) shows a decision tree structure that was preferred just once out of 10 trees in the forest. We learn from the figures that area, precipitation, and river length are second in importance (revealed by their occurrence at the second level). At the third level two new predictors are included – the temperature and the k-factor, making them the third most important variables. The slope index, area and river also accompany them, again signifying their importance in the model.

The R^2 achieved by the prediction algorithm was (>88%) for all the testing sessions. Multiple training and testing sessions helped check the robustness of the algorithm and it was found that the accuracy was consistent at 88% or more. The unchanging decision tree structures throughout the testing sessions further attested to the dependency among the predictor variables. Table 3 shows the result of training and testing of the RFQR on the dataset.

c. SHAP interpretation and predictor importance

In Figure 8, we see a bee swarm plot showing the strength of various input predictors in predicting the output variable. The Y-axis lists the different predictors while the corresponding area in the graph shows how strongly (via SHAP values), the predictor contributed towards the predicted target. For every predictor we have 1000 dots corresponding to the 1000 test data points. The adjoining color bar gives a qualitative description of the magnitude of the target (recoveriness) variable, and the X-axis gives the numerical value (SHAP) of the input predictor. It can be seen that slope index (si) has a wider spread and occurs at the top in the Y-axis. The spread indicates that this predictor is more informative of the target. Towards the bottom, in the axis, is the basin texture which is least informative as evident from its concentrated occurrences for all the 1000 test data points.

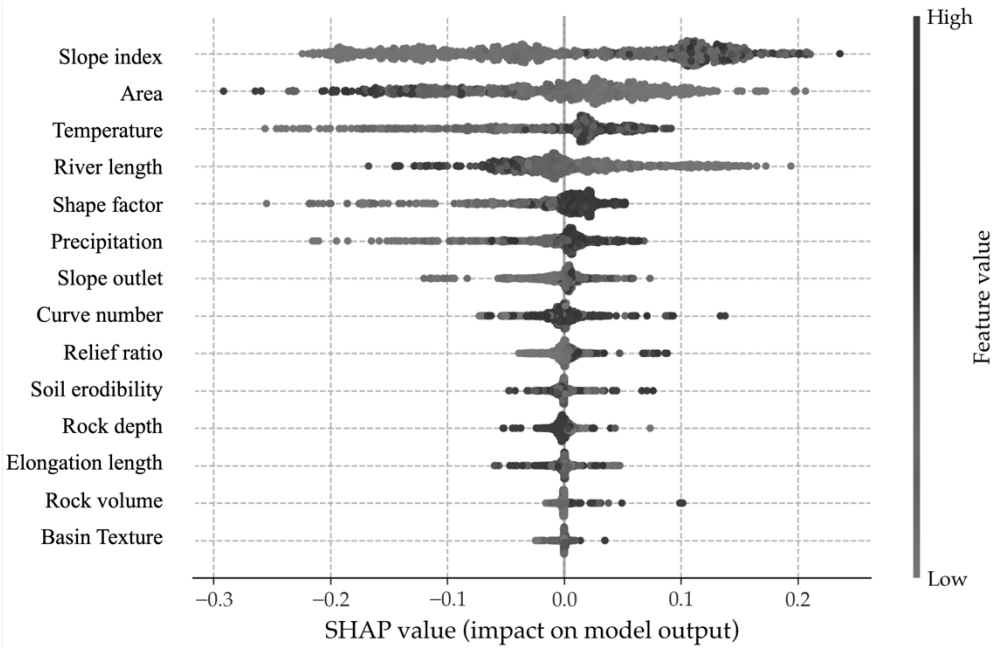

Fig. 8. Bees plot showing the strength of different predictors in predicting 1000 random values of Recoveriness. Each predictor in the Y-axis has 1000 dots in the graph area. The color bar shows the SHAP value of the predictor used to predict the target value to achieve an overall R^2 of 89%. Again, slope index (si) happens to be the most important variable seconded by temperature, area and river length.

Figure 8 gives us the idea of the predictors in decreasing order of informative-ness. The contribution of basin texture input is negligible with the rock volume being just marginally better than the previous. The temperature, area and river length are second most important input predictors after slope index in predicting recoveriness.

A grid search of hyperparameters was done for the Random Forest algorithm. The result of the best performing model has been reported in this section. The trained model is used to make the predictions of recoveriness over the CONUS. The three hyperparameters of the regression algorithm were, 1) *max_depth*, which determines the maximum levels allowed during the bifurcation of the decision space, 2) *max_features*, a parameter whose value must be less than the total number of predictors, determines the maximum number of predictors that can be used for building the bootstrap dataset, and 3) *number_of_trees*, which determines the total number of weak estimators to build the ensemble model. The *max_depth* hyperparameter was specified to restrict the decision tree formation with only 7 levels (half the total predictors) in the hierarchy. The *max_features* is set to total number of predictors, i.e., 14, effectively allowing the algorithm to consider all the predictors but with only 7 levels of complexity in relationship. The tree plot in Figure 7 shows only the first 3 levels of the hierarchy. The *number_of_trees* is fixed at value 10 so as not to promote over-complicated models.

The spatial resolution for the prediction dataset used to estimate recoveriness over the U.S. is 1 km. Plot of the predicted "Recoveriness" is shown in Figure 9. Recoveriness values range from 0 to 1. Regions of high recoveriness are identified as red ; the green and blue regions indicate regions of low recovery (bad). The Southern part in the map shows high values of recoveriness. Referring to Figure 2, the regions with a high recovery can be identified as the Appalachians, Missouri Valley, and the Flash Flood Alley. The northern parts of Arizona and the Front range are mostly characterized by low recovery. The eastern parts of the West Coast show similarly low recovery regions.

Figure 9b) shows the associated uncertainty associated with the estimated recoveriness. The uncertainty is defined as the "Prediction Interval Width", where the width is given using the following Equation (5):

$$Predicted\ Interval\ Width = 95\%\ quantile\ -\ 5\%\ quantile \quad (5)$$

Uncertainty is indicated by the darker, blueish regions. In other words, the predicted interval was wider in those regions, i.e., the model was not as sure as the lighter regions in predicting the recoveriness. The uncertainty does not seem to show any pattern except some dark regions at the center and southwest direction. Both the plots help us to identify the hotspots of high and low recoveriness in an ungauged region, inclusive of the associated uncertainty in the prediction.

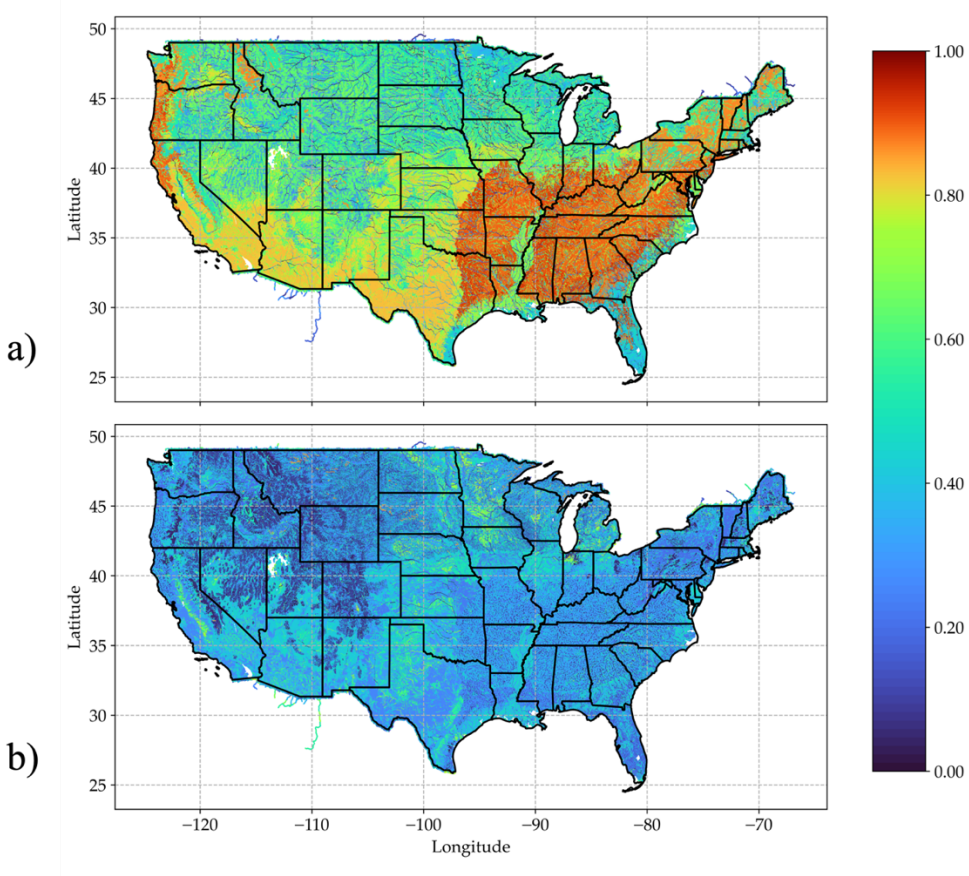

Fig. 9. a) High density prediction of Recoveriness across the USA. The red regions mark the areas with short recovery times while the green and blue regions indicate areas with longer recovery times. b) Uncertainty plot of "Recoveriness": The blueish parts indicate regions with high certainty. The plot shows the 95% prediction interval width.

High recovery regions show specific patterns – clinging to the western shoreline and running along the inlands of Sierra Nevada are situated the highlands, consistent with Figure 2. Same potential for recoveriness can be associated with Arizona . High recovery potential can also be observed in the region extending from the southeast Arizona to the Mogollon Rim. .

The predictions in the map clearly indicate high recoveriness zones extending from southwest Texas to Kansas, Arkansas, Oklahoma, and Missouri. Worth noting in the predictions is the revelation of high recovery regions of the western slopes of the Appalachians consisting of Kentucky, Tennessee, and west Virginia .

d. Correlation between flashiness and recoveriness

Figure 10a) displays the relationship between recoveriness and flashiness, which mapping consistency over the U.S. has been indirectly validated by (Saharia et al., 2017b). One can note that the two variables display a strong relationship, suggesting that similar hydrologic processes are at stake for the two variables.

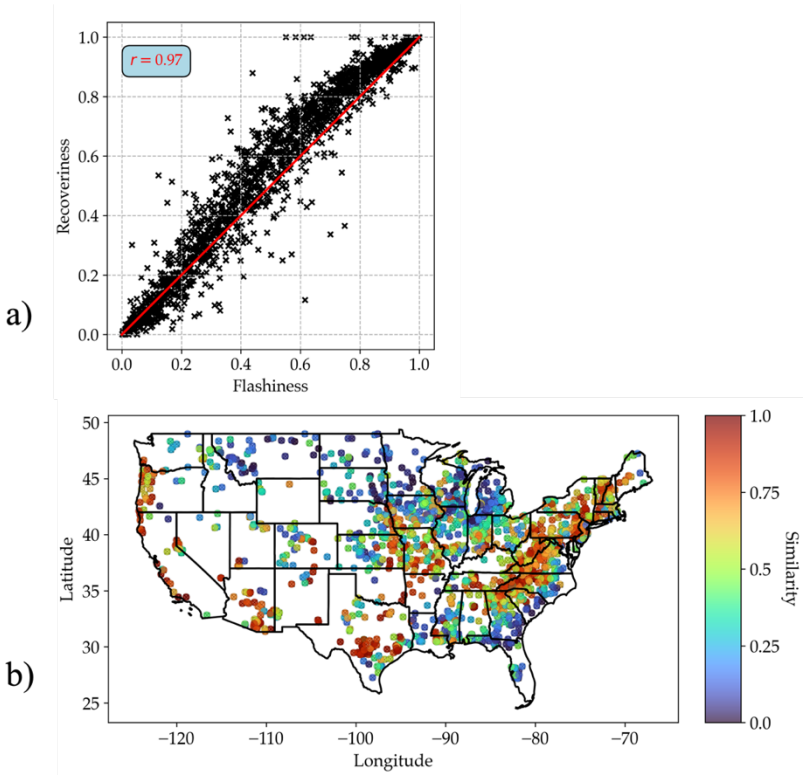

Fig. 10. a) A plot showing the correlation between flashiness and recoveriness. The relation is nonlinear although there exists a high degree of correlation. b) Spatial distribution of recoveriness over the CONUS – Higher values indicate quick recovery times and vice-versa.

For flashiness values less than 0.2, there is a linear rise in recoveriness. For higher values greater than 0.2, a second-degree polynomial would be a better fit. Fitting that gives the following equation:

$$y = -0.34x^2 + 1.38x - 0.03 \quad (6)$$

where, y represents recoveriness and x represents flashiness. The equation indicates a weakly nonlinear relationship between the two. Figure 10b) gives the spatial plot of recoveriness, where higher values indicate quick recovery while lower values are indicative of delayed recovery. Basins that can quickly concentrate flows and result in high flashiness, are also associated with a high recoveriness. the consistency of the flashiness mapping over the U.S. has been qualitatively established in Saharia et al. (2017b).

511

512 5. Conclusions

513 This study fucuses on a recession period of a flood, a less explored area of research as
514 compared to the rising flood period. The dataset used in this study contains a number of
515 climatological and geomorphological information along with details of flooding event
516 spanning 78 years from the gauged region. The dependency of geomorphological variables
517 and climatology on recovery period has been explored in this work following which a new
518 variable called "recoveriness" is introduced in this paper, which measures the flood recovery
519 times, and is a combination of peak as well as recession period. We have found that
520 "recoveriness" is a highly nonlinear variable and bears a complex relationship with the
521 geomorphological and climatological predictors. The results are supported by suitable
522 machine learning models that predict recoveriness at every ungauged location across the
523 CONUS. The main findings of this study are:

524 1. There exists a high correlation between the flood recovery times and the basin
525 properties and topology. For example, the slope of the basin happens to be highly
526 correlative with recovery and this is quite reasonable acknowledging the fact that
527 steep slopes tend to cause faster runoffs needing lesser recovery times. Similarly,
528 basins with a smaller area would require less time because there is less water to
529 disperse.

530 2. Six hotspots with high recoveriness spanned the United States: the Arizona, the Front
531 Range, West Coast, the Missouri Valley, Flash Flood Alley, and the Appalachian
532 Mountains.

533 3. Machine learning model was used to predict the recoveriness values using a highly
534 dense data containing ungauged region over the CONUS. Several new localized
535 hotspots were identified: the western slopes of the Appalachians consisting of the
536 Kentucky, Tennessee, and west Virginia and the interlinked areas of eastern Montana,
537 and northern Idaho.

538 This paper develops a comprehensive climatological perspective on flood recovery. In a
539 future work, we see the potential to establish an event-level "recoveriness" metric that could
540 facilitate a deeper understanding of the post-flood recovery process. Overall, this new metric
541 has the potential to be adopted for disaster risk reduction efforts.

Acknowledgments.

This research was conducted in the HydroSense lab (https://hydrosense.iitd.ac.in/) of IIT Delhi and the authors acknowledge the IIT Delhi High Performance Computing facility for providing computational and storage resources. Dr. Manabendra Saharia gratefully acknowledges financial support for this work through grants from ISRO Space Technology Cell (STC0374/RP04139); MoES Monsoon Mission III (RP04574); and IC-IMPACTS (RP04558).

Conflicts of Interest.

The authors declare that they have no known competing financial interests or personal relationships that could have appeared to influence the work reported in this paper.

Data Availability Statement.

The data that support the findings of this study are openly available in the repository titled "Mapping a novel metric for Flash Flood Recovery using Interpretable Machine Learning" at https://zenodo.org/doi/10.5281/zenodo.10090794.

REFERENCES

Ahmad, A., A. El-Shafie, S. F. M. Razali, and Z. S. Mohamad, 2014: Reservoir optimization in water resources: a review. *Water resources management*, **28**, 3391–3405.

Alfieri, L., and J. Thielen, 2015: A European precipitation index for extreme rain-storm and flash flood early warning. *Meteorological Applications*, **22**, 3–13.

Amaya, M., N. Linde, and E. Laloy, 2022: Hydrogeological multiple-point statistics inversion by adaptive sequential Monte Carlo. *Advances in Water Resources*, **166**, 104252.

Amit, H., V. Lyakhovsky, A. Katz, A. Starinsky, and A. Burg, 2002: Interpretation of spring recession curves. *Ground Water*, **40**, 543.

569 Ao, Y., H. Li, L. Zhu, S. Ali, and Z. Yang, 2019: The linear random forest algorithm and its
570 advantages in machine learning assisted logging regression modeling. *Journal of*
571 *Petroleum Science and Engineering*, **174**, 776–789.

572 Babagoli, M., M. P. Aghababa, and V. Solouk, 2019: Heuristic nonlinear regression strategy
573 for detecting phishing websites. *Soft Computing*, **23**, 4315–4327.

574 Baker, D. B., R. P. Richards, T. T. Loftus, and J. W. Kramer, 2004: A new flashiness index:
575 Characteristics and applications to midwestern rivers and streams 1. *JAWRA Journal of*
576 *the American Water Resources Association*, **40**, 503–522.

577 Berz, G., 2000: Flood disasters: lessons from the past—worries for the future. *Proceedings of*
578 *the institution of civil engineers-water and maritime engineering*, Vol. 142 of, Thomas
579 Telford Ltd, 3–8.

580 Bhaskar, N. R., M. N. French, and G. K. Kyiamah, 2000: Characterization of flash floods in
581 Eastern Kentucky. *Journal of hydrologic engineering*, **5**, 327–331.

582 Biswal, B., and M. Marani, 2010: Geomorphological origin of recession curves. *Geophysical*
583 *Research Letters*, **37**.

584 Buschjäger, S., P.-J. Honysz, and K. Morik, 2022: Randomized outlier detection with trees.
585 *International Journal of Data Science and Analytics*, **13**, 91–104.

586 Chang, C., and P. Feng, 2017: The impact of land use/land cover changes and hydraulic
587 structures on flood recession process. *Journal of Water and Climate Change*, **8**, 375–387.

588 Chapman, T., 1999: A comparison of algorithms for stream flow recession and baseflow
589 separation. *Hydrological Processes*, **13**, 701–714.

590 Costa, J. E., 1987: A comparison of the largest rainfall-runoff floods in the United States with
591 those of the People's Republic of China and the world. *Journal of Hydrology*, **96**, 101–
592 115.

593 Costa, M. H., A. Botta, and J. A. Cardille, 2003: Effects of large-scale changes in land cover
594 on the discharge of the Tocantins River, Southeastern Amazonia. *Journal of hydrology*,
595 **283**, 206–217.

596 Diakakis, M., G. Deligiannakis, Z. Antoniadis, M. Melaki, N. Katsetsiadou, E. Andreadakis,
597 N. Spyrou, and M. Gogou, 2020: Proposal of a flash flood impact severity scale for the
598 classification and mapping of flash flood impacts. *Journal of hydrology*, **590**, 125452.

599 Douben, K.-J., 2006: Characteristics of river floods and flooding: a global overview, 1985–
600 2003. *Irrigation and Drainage: The journal of the International Commission on*
601 *Irrigation and Drainage*, **55**, S9–S21.

602 Gimeno, M., K. Sada del Real, and A. Rubio, 2023: Precision oncology: a review to assess
603 interpretability in several explainable methods. *Briefings in Bioinformatics*, bbad200.

604 Gourley, J. J., and Coauthors, 2013: A unified flash flood database across the United States.
605 *Bulletin of the American Meteorological Society*, **94**, 799–805.

606 Huan, J., H. Li, M. Li, and B. Chen, 2020: Prediction of dissolved oxygen in aquaculture
607 based on gradient boosting decision tree and long short-term memory network: A study of
608 Chang Zhou fishery demonstration base, China. *Computers and Electronics in*
609 *Agriculture*, **175**, 105530.

610 Islam, S. R., W. Eberle, and S. K. Ghafoor, 2020: Towards quantification of explainability in
611 explainable artificial intelligence methods. *The thirty-third international flairs*
612 *conference*.

613 John, G. H., 1995: Robust Decision Trees: Removing Outliers from Databases. *KDD*, Vol. 95
614 of, 174–179.

615 Joshi, R. M., A. Kumar, and K. H. Singh, 2023: A simulation and data informed approach to
616 porosity partitioning. *Geoenergy Science and Engineering*, **229**, 212044,
617 https://doi.org/10.1016/j.geoen.2023.212044.

618 Khaleghi, M., V. Gholami, J. Ghodusi, and H. Hosseini, 2011: Efficiency of the
619 geomorphologic instantaneous unit hydrograph method in flood hydrograph simulation.
620 *Catena*, **87**, 163–171.

621 Kumar, A., R. Shrivastava, and K. Singh, 2020: Bayesian inference of material properties in
622 disordered media using sound characteristics. *Europhysics Letters*, **129**, 24001.

623 Kuntla, S. K., M. Saharia, and P. Kirstetter, 2022: Global-scale characterization of
624 streamflow extremes. *Journal of Hydrology*, **615**, 128668.

625 Liu, P., L. Li, S. Guo, L. Xiong, W. Zhang, J. Zhang, and C.-Y. Xu, 2015: Optimal design of
626 seasonal flood limited water levels and its application for the Three Gorges Reservoir.
627 *Journal of Hydrology*, **527**, 1045–1053.

628 Lundberg, S. M., and S.-I. Lee, 2017: A Unified Approach to Interpreting Model Predictions.
629 *Advances in Neural Information Processing Systems 30*, I. Guyon, U.V. Luxburg, S.
630 Bengio, H. Wallach, R. Fergus, S. Vishwanathan, and R. Garnett, Eds., Curran
631 Associates, Inc., 4765–4774.

632 Marcuzzi, F., C. Lucchese, and S. Orlando, 2022: Filtering out outliers in learning to rank.
633 *Proceedings of the 2022 ACM SIGIR International Conference on Theory of Information*
634 *Retrieval*, 214–222.

635 Meinshausen, N., and G. Ridgeway, 2006: Quantile regression forests. *Journal of machine*
636 *learning research*, **7**.

637 Nanfack, G., P. Temple, and B. Frénay, 2022: Constraint Enforcement on Decision Trees: A
638 Survey. *ACM Computing Surveys (CSUR)*, **54**, 1–36.

639 Nathan, R. J., and T. A. McMahon, 1990: Evaluation of automated techniques for base flow
640 and recession analyses. *Water resources research*, **26**, 1465–1473.

641 Ortega, K. L., T. M. Smith, K. L. Manross, K. A. Scharfenberg, A. Witt, A. G. Kolodziej, and
642 J. J. Gourley, 2009: The severe hazards analysis and verification experiment. *Bulletin of*
643 *the American Meteorological Society*, **90**, 1519–1530.

644 Panjei, E., L. Gruenwald, E. Leal, C. Nguyen, and S. Silvia, 2022: A survey on outlier
645 explanations. *The VLDB Journal*, **31**, 977–1008.

646 Pielke, R. A., and M. W. Downton, 2000: Precipitation and damaging floods: Trends in the
647 United States, 1932–97. *Journal of climate*, **13**, 3625–3637.

648 Potdar, A. S., P.-E. Kirstetter, D. Woods, and M. Saharia, 2021: Toward predicting flood
649 event peak discharge in ungauged basins by learning universal hydrological behaviors
650 with machine learning. *Journal of Hydrometeorology*, **22**, 2971–2982.

651 Rentschler, J., M. Salhab, and B. A. Jafino, 2022: Flood exposure and poverty in 188
652 countries. *Nature communications*, **13**, 3527.

653 Saharia, M., P.-E. Kirstetter, H. Vergara, J. J. Gourley, and Y. Hong, 2017a: Characterization
654 of floods in the United States. *Journal of Hydrology*, **548**, 524–535.

655 ——, ——, ——, ——, ——, and M. Giroud, 2017b: Mapping flash flood severity in the
656 United States. *Journal of Hydrometeorology*, **18**, 397–411.

——, ——, ——, ——, I. Emmanuel, and H. Andrieu, 2021: On the impact of rainfall spatial variability, geomorphology, and climatology on flash floods. *Water Resources Research*, **57**, e2020WR029124.

Schwarz, G. E., and Alexander R. B., 1995: *Soils data for the Conterminous United States Derived from the NRCS State Soil Geographic (STATSGO) Data Base*. U.S. Geological Survey, https://water.usgs.gov/lookup/getspatial?ussoils.

Shixiang, F., and H. Shaowen, 1991: Testing research on the effects of land surface slopes upon surface runoff. *Bulletin of Soil and Water Conservation (China)*,.

Shorr, N., 2000: Early utilization of flood-recession soils as a response to the intensification of fishing and upland agriculture: Resource-use dynamics in a large Tikuna community. *Human Ecology*, **28**, 73–107.

Shuster, W., Y. Zhang, A. Roy, F. Daniel, and M. Troyer, 2008: Characterizing Storm Hydrograph Rise and Fall Dynamics With Stream Stage Data 1. *JAWRA Journal of the American Water Resources Association*, **44**, 1431–1440.

Yan, B., F. Ren, M. Cai, and C. Qiao, 2020: Bayesian model based on Markov chain Monte Carlo for identifying mine water sources in Submarine Gold Mining. *Journal of Cleaner Production*, **253**, 120008.

Ye, R., Y. He, S. Yu, and Z. Song, 2019: Effects of recent morphodynamic evolution on flood regimes in the Pearl River Delta. *Natural Hazards*, **96**, 1091–1119.

2019: *National Weather Service Manual*. https://www.nws.noaa.gov/directives/sym/pd01009050curr.pdf.

2022: *NWS Annual Flood Loss Summary Report*. NWS Annual Flood Loss Summary Report, https://www.weather.gov/media/water/WY2022_Flood_Loss.pdf.